



Energy-Saving Electrochemical Hydrogen Production on Dynamic Hydrogen Bubble-Template Electrodeposited Ni-Cu-Mn Nano-Micro Dendrite

N. Lotfi and Gh. Barati Darband^z 

Materials and Metallurgical Engineering Department, Faculty of Engineering, Ferdowsi University of Mashhad, Mashhad 91775-1111, Iran

Replacing an oxidation reaction with lower potential than OER can significantly reduce the cell potential in the hydrogen production process. Here, we synthesized Ni-Cu-Mn alloy nano-micro dendrites using one-step and binder-free dynamic hydrogen bubble template (DHBT) electrochemical deposition method and studied its activity for urea oxidation reaction (UOR) and hydrogen evolution reaction (HER). Electrochemical results for HER represented that the η_{10} for the optimized electrode is 63 mV and its Tafel slope is 111 mV.dec⁻¹. Also, the results of polarization tests showed that by replacing the OER process with UOR, in the overall water splitting process, to create a current density of 10 mA.cm⁻² the cell potential reaches 1.361 V, which is 179 mV less than HER-OER. Also, the results of electrocatalytic stability represented small changes in overpotential during the electrolysis process, which indicates the unique electrocatalytic stability. The improvement of electrocatalytic results in this study is due to the fabrication of a binder-free and three-dimensional surface as well as the synergistic effect caused by elements in improving the intrinsic electrocatalytic activity. This study revealed that the use of DHBT method can be used effectively to synthesizing active and cost-effective bi-functional electrocatalysts for HER-UOR.

© 2022 The Electrochemical Society ("ECS"). Published on behalf of ECS by IOP Publishing Limited. [DOI: [10.1149/1945-7111/ac8d30](https://doi.org/10.1149/1945-7111/ac8d30)]

Manuscript submitted June 21, 2022; revised manuscript received July 27, 2022. Published September 7, 2022.

Supplementary material for this article is available [online](#)

Widespread consumption of fossil fuels and severe environmental problems have led the special attention being paid to the production of clean and renewable fuels. Among renewable fuels, hydrogen is considered as a future energy carrier due to its high energy density, cleanliness and abundance of production sources.¹ There are several methods for producing hydrogen, in particular, the production of molecular hydrogen through the electrochemical water splitting is an attractive solution.²⁻⁴ In electrochemical water splitting, hydrogen and oxygen are produced at the surface of cathode and anode, respectively.⁵⁻⁸ Despite the major advantages of this method, due to the slow kinetics that results from different resistances in the electrochemical water splitting process, the electrochemical hydrogen production is not yet economical, which prevents the widespread industrial using of this method. As mentioned, electrochemical water splitting consists of two processes, HER and OER. OER is a kinetically sluggish reaction that involves a four-electron electrochemical oxidation step which leads to large energy consumption in electrochemical water splitting process.⁹ Therefore, focusing on anodic process optimization plays an essential role in improving process efficiency and reducing overall cell potential. One method to improve the anodic process is to fabrication of electrocatalysts that can reduce the OER overpotential, which has been extensively studied recently. However, one effective manner is to replace an anodic reaction with less theoretical potential than OER.¹⁰⁻¹² Recently, alternatives oxidation reaction such as urea,¹³ hydrazine,¹⁴ methanol¹⁵ and ethanol¹⁶ oxidation reaction have been proposed to improve hydrogen production efficiency. Among these reactions, urea oxidation reaction (UOR) ($\text{CO}(\text{NH}_2)_2 + \text{H}_2\text{O} \rightarrow \text{N}_2 + 3\text{H}_2 + \text{CO}_2$) has been considered recently due to its high energy density, non-toxicity and low price.¹⁷ UOR has lower thermodynamic voltage (0.37 V) than water electrolysis (1.23 V) and the reaction products are only CO_2 and N_2 . Despite the stated advantages, unfortunately the UOR process is a 6-electron transfer process, which reduces the reaction kinetics.¹⁸ Therefore, it is necessary to conduct research on the development of active electrode materials for improvement the UOR process.

It is confirmed that precious metals have excellent properties for in HER and UOR. For example, Pt and Pd have outstanding activity

for HER and IrO_2 and RuO_2 for OER and UOR. However, the high price and insufficient reserves of these electrodes have limited their widespread usage.^{19,20} Recently, some cost-effective and highly active catalysts such as MnO_2 nanocrystals²¹ and $\text{Ni}(\text{OH})_2$ nanotubes²² have been proposed to improve the UOR process. But many of them are not good electrocatalysts for HER. Therefore, it is vital to synthesize an electrocatalyst that can work well for HER and UOR at the same time. By tailoring the electronic and structural properties of transition metal-based catalysts, the desired electrocatalytic activity can be achieved.

In addition, the performance of the processes in which the gas evolves from the electrode surface is strongly dependent on the microstructure and morphology of the catalyst. The rational microstructure design of an electrode, such as the formation of nanocones²³ and nano-micro dendrites,²⁴ improves the electrocatalytic properties by optimizing ion penetration, mass transfer and gas detachment. According to recent studies, transition metal-based active materials such as transition metal oxides,²⁵ hydroxides,²⁶ alloy²⁷ selenides,^{13,28} phosphides²⁹ and sulfides³⁰⁻³² have been considered in alkaline environments for UOR or HER/UOR for their excellent properties like cost-effectiveness, availability, and excellent electrocatalytic properties. In the meantime, we can create transition metallic-based electrocatalyst by binder-free electrochemical deposition method in three dimensions and nanostructure manner. Because, electronic properties of three-dimensional metallic alloy electrodes can be improved by alloying, and by three-dimensionality, the active surface area can be improved, and also mass transfer is facilitated easily. So, nanostructured and 3-dimensional metallic alloyed are good candidates for accelerating UOR and HER processes. On the other hand, creating binder-free and in-situ electrodes using electrochemical deposition method for using in supercapacitors, batteries, electrocatalysts and photoelectrocatalysts have numerous advantages that have attracted a lot of attention.³³⁻³⁵ In other methods, catalytic powders are physically mixed with polymer binder materials and coated on the substrate for electrochemical testing, resulting in poor stability and performance. Therefore, electrodes made by electrochemical deposition method usually have better stability and electrocatalytic properties.³⁶ Recent studies have shown that addition of a second or third alloying element can lead to substantial improvement in electrocatalytic activity, among which the Mn has a surprising effect by changing the electronic structure of catalysts.³⁷⁻⁴⁰ For

^zE-mail: baratidarband@um.ac.ir

example, our recent study showed that Mn doping in the Ni-Se structure has a significant effect on improving electrocatalytic activity for HER and UOR.¹³ Among electrochemical deposition methods, the dynamic hydrogen bubble template (DHBT) method can be useful due to its high deposition rate and ability to form micro-nano dendrites.⁴¹ Various alloying system can be deposited using this method. To the best of our knowledge, the Ni-Cu-Mn ternary alloy has not yet been created using the DHBT method. So, it is expected that Ni-Cu-Mn micro-nano dendritic three-dimensional alloy can have excellent electrocatalytic activity for HER and UOR. Therefore, electrochemical deposition of three-dimensional Ni-Cu-Mn electrocatalyst by DHBT method in different coating conditions and investigation of its electrocatalytic behavior for HER-UOR and OER processes to improve the hydrogen production efficiency are the aim of this study.

Experimental

Fabrication of electrodes.—We synthesized Ni-Cu-Mn micro-nano dendrites on the nickel foam (NF) substrate by one-step DHBT electrochemical deposition method. Schematic of coating formation in is shown Fig. 1. Initially, we degreased NF ultrasonically in ethanol for 15 min and then activation was performed in 20% HCl for 30 s. The coating formation was performed by a two-electrode system in which the prepared NF sample was used as the cathode and graphite rod as the anode. The coating bath composition includes 0.5 M $\text{NiSO}_4 \cdot 6\text{H}_2\text{O}$, 0.01 M $\text{CuSO}_4 \cdot 5\text{H}_2\text{O}$, 1.0 M HCl, 1.5 M H_2SO_4 and different concentrations of MnCl_2 (10, 30, 50, 70 and 100 g.l^{-1}). The applied current density for coating formation was 2 A.cm^{-2} and the time for coating treatment was 100 s in room temperature. All materials used in this study were analytical grade. After coating process, the samples washed with distilled water and kept in a desiccator for further studies.

Characterization.—We investigated the morphology and chemical composition of coatings by field emission scanning electron microscopy equipped with energy dispersive spectroscopy (EDS) (FESEM, MIRA3 TESCAN). Also, the phase structure of the coatings was analyzed by X-ray diffraction analysis (XRD), $\lambda = 40.15406$, step size = 0.02 and time per step = 1 s (Philips, Netherlands).

ZIVE-SP1 potentiostat was employed for electrochemical characterization which was carried out in a three-electrode configuration in which the synthesized electrode used as the working electrode, the Ag/AgCl used as the reference electrode, and the graphite rod as the counter electrode. We performed electrochemical studies for HER and OER in 1.0 M KOH solution and for UOR in 1.0 M KOH +

0.5 M urea solution. For investigating the electrocatalytic behavior, linear sweep voltammetry (LSV) method was employed with a scan rate of 5 mV.s^{-1} . The obtained electrochemical potentials were converted to RHE by the following equation:

$$E_{\text{RHE}} = E(\text{vs Hg/HgO}) + E_{\text{Hg/HgO}} + 0.0592 \text{ pH.} \quad [1]$$

In addition, electrochemical impedance spectroscopy (EIS) was performed in the frequency range between 100 kHz to 100 mHz at different overpotentials for better understanding of electrocatalytic kinetic and mechanism. Long-term electrocatalytic stability was determined by chronopotentiometry (CP) at applied current densities of 100 mA.cm^{-2} and cyclic voltammetry (CV) after 1000 cycles with the scan rate of 100 mV.s^{-1} . Electrochemically active surface area (ECSA) was obtained by CV test in areas with none-faradic current and at different scan rates. Here, the current density vs scan rate slope represents the value of double-layer capacitance (C_{dl}). By dividing this value by the double-layer capacitance of a smoothly atomic surface, the value of ECSA is obtained.

Results and Discussion

Electrodeposition and characterization of Ni-Cu-Mn.—After a one-step electrochemical deposition process, the NF silver color changed to black brown (Fig. S1 (available online at stacks.iop.org/JES/169/096508/mmedia)), indicating that a new material successfully deposited on the NF surface. In order to determine the optimal concentration of Mn ions, different concentrations of 10–100 g.l^{-1} of MnCl_2 were used in the coating bath. Initially, we explored the morphology and microstructure of different samples by FESEM. The FESEM images at various magnifications related to the Ni-Cu electrode is shown in Figs. 2a–2c. Fig. 2a shows that the coating is uniformly formed throughout the NF and also, Fig. 2b shows cavities with 25–50 μm in size due to the increase in applied cathodic current density during coating formation and therefore intense hydrogen evolution (DHBT method). Due to the high cathodic current density, two general processes occur in the DHBT method that lead to the formation of the 3-dimentional nano- microstructure coating. The first is metal deposition process from the bath containing metallic ions. In this study we used Ni, Cu and Mn ions. So, the metallic deposition processes are as follows:

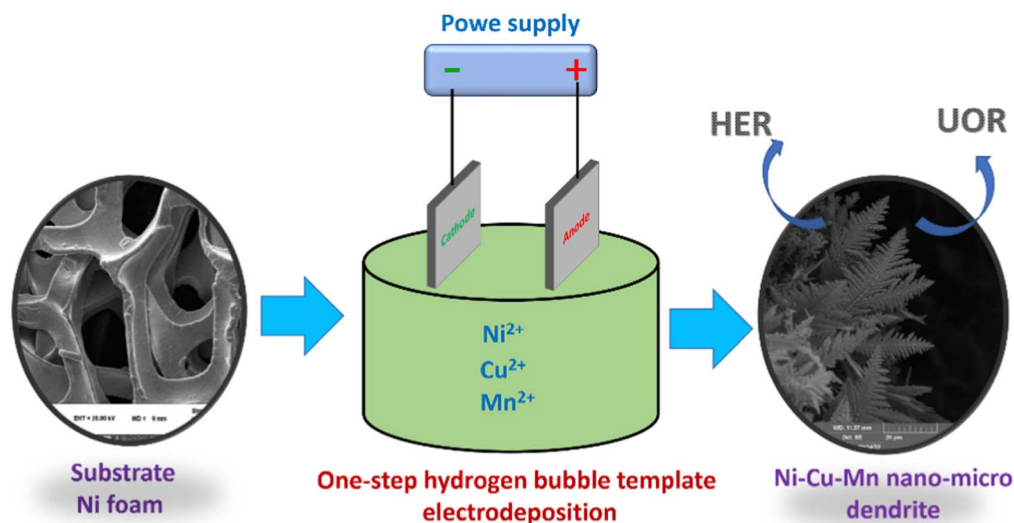
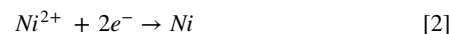


Figure 1. Schematic representation of coating formation.

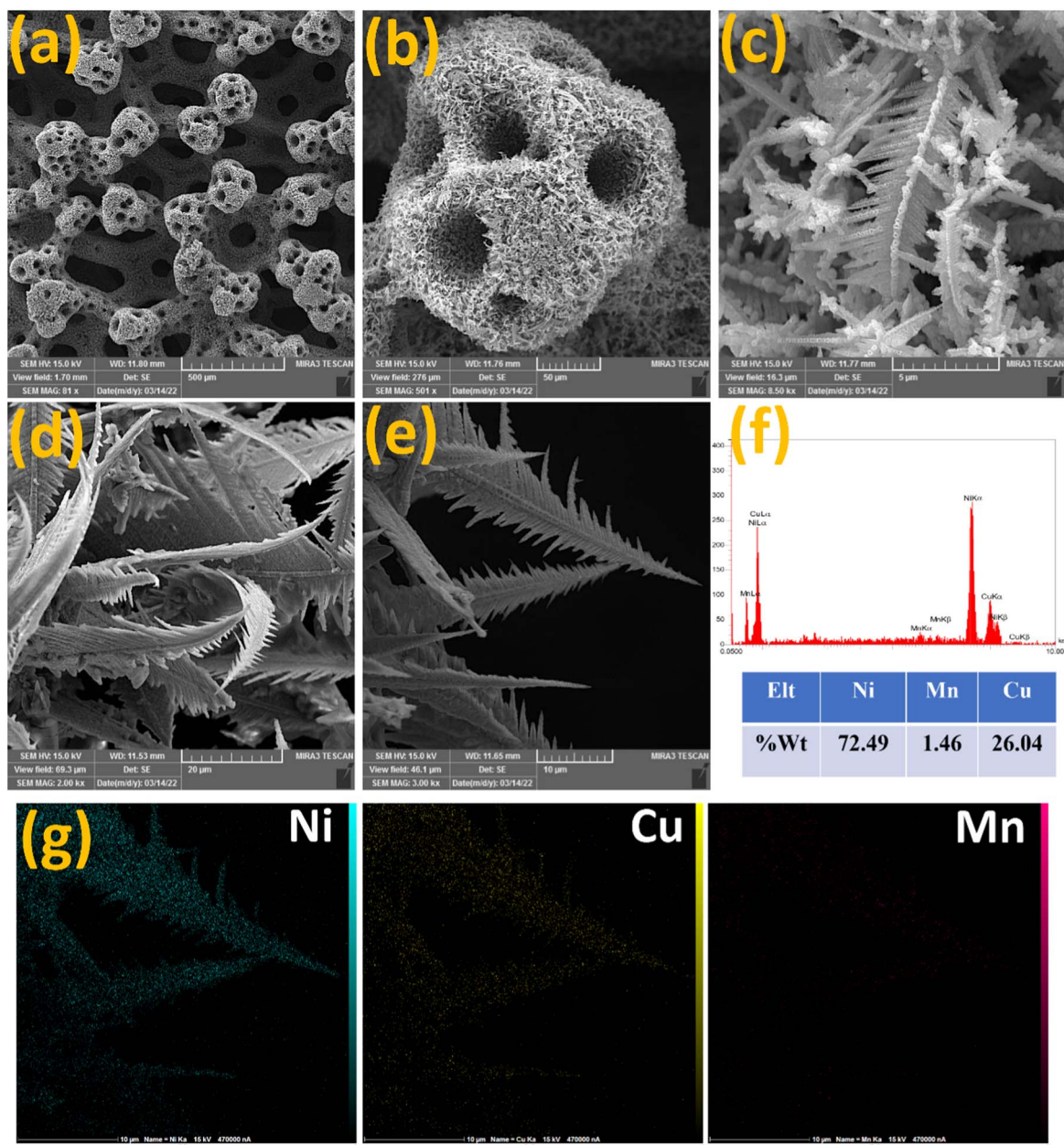


Figure 2. (a)–(c) Low and high magnification images of Ni-Cu electrode, (d) and (e) FESEM images of Ni-Cu-Mn electrode, (f) EDS result of Ni-Cu-Mn electrode fabricated in bath with 70 g.lit⁻¹ MnCl₂ and (g) elemental mapping of Ni-Cu-Mn electrode.



The second process involves the hydrogen evolution reaction at the cathode surface in the acidic environment as follow:



The principle of DHBT is that the generated hydrogen bubbles affect the growth of the metallic layer and act as a dynamic template for the electrochemical deposition process.⁴² Due to the high overpotential, supersaturation of H₂ in the solution near the electrode leads to heterogeneous nucleation of bubbles on the surface. As long as the bubbles are stuck to the electrode surface, small bubbles combine to formation of large bubbles. When the bubbles reach a critical size (bubble break-off diameter), they separate from the electrode surface.^{43,44} Bubbles that adhere to the electrode surface and detach from the surface disrupt the surface and thus affect the electrochemical deposition of metallic coatings. Hydrogen bubbles block

active surface sites for metallic ions deposition, forcing metallic ions to find other deposition sites around the bubbles. At the critical size, the bubble detaches from the electrode surface and, therefore, a hole is formed in the surface. The coating on the surface will grow around these bubbles, and the bubbles will act as a dynamic template. Now, we will look at how dendrites form in the DBHT process. From Fig. 2c, we can clearly observe micro-nano dendrites which formed at high applied current densities. These dendrites are usually formed when the electrochemical deposition process is under diffusion control. Initially, a large number of nuclei will form as soon as sufficient potential and current are applied. Over time, deposition continues with the incorporation of newly adsorbed atoms at the surface of the pre-formed nuclei. With duration of time, the concentration of electro-active species in the front of the growth depletes rapidly, and as a result the newly deposited particles are more likely to attach to the tip of the clusters to other parts of the clusters which leads to the external growth of the clusters. As deposition continues, tertiary clusters grow at the surface of the

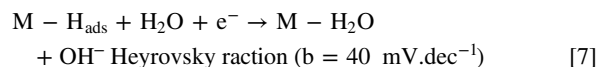
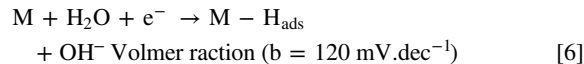
secondary clusters, which results in the final dendritic structure. Primary trunks and clusters usually grow in certain preferential directions.

Also, the FESEM images of the coated electrodes at different concentrations of Mn ions are represented in Fig. S2 and the FESEM image of the electrode fabricated at 70 g.l^{-1} MnCl_2 is shown in Figs. 2d and 2e. It is observed that the morphology is almost constant and dendritic in all concentrations. Therefore, it can be said that the concentration of Mn ions had little effect on morphology. The EDS results for the different samples is shown in Fig. S3 as well as the EDS analysis of the electrode fabricated at 70 g.l^{-1} MnCl_2 is shown in Fig. 2f. It is clearly observed that the atoms which contribute to coating formation are Ni, Cu and Mn, which indicates the successful reduction and presence of all elements in the coating. EDS analysis also shows with increasing concentration of Mn ions in the coating bath, the amount of Mn ions absorbed in the coating increases and reaches 1.46% at 70 g.l^{-1} and 1.48% at 100 g.l^{-1} which has remained almost constant. Also, the results of elemental mapping analysis (given in Fig. 2g), obviously indicates elements participated uniformly in all parts of the coating, which confirms the successful participation of all elements in the deposit formation, as well as the formation of a solid solution.

The results of XRD analysis of Ni-Cu and Ni-Cu-Mn electrode fabricated in the bath with 70 g.l^{-1} MnCl_2 to investigate the phase structure are shown in Fig. 3. Based on XRD pattern of Ni-Cu electrode, it can be seen that pattern consist of diffraction peaks located at $2\theta = 44.9^\circ$, 52.2° and 76.6° which are the diffraction peaks of (111), (200) and (220) of Ni facets, respectively. Obviously, there was not any diffraction peaks for Cu which confirms the formation of Ni-Cu solid solution. With the addition of Mn atoms to the Ni-Cu coating structure, the position of main peaks move towards lower 2θ values, which is due to the replacement of Mn atoms in the Ni-Cu crystal structure. In general, when an element is doped in the another crystalline structure, the host crystalline structure becomes disordered, and if the radius of the doped atom is larger than the radius of the host lattice, the lattice parameter is locally increased, which leads to the shift of peaks to lower values of 2θ .^{45,46} Since the radius of Mn atoms is larger than that of Ni, therefore, Mn doping leads to a peak shift towards lower 2θ values. In addition, no separate Mn peak is formed due to the contribution of Mn, which also confirms the formation of a solid solution.

Electrochemical hydrogen evolution reaction.—We examined the catalytic behavior of synthesized electrodes under different

conditions in a three-electrode system by the LSV method at a scanrate of 5 mV.s^{-1} in alkaline solution, initially. In this study, the needed potentials to create current densities of 10 and 100 mA.cm^{-2} are shown as η_{10} and η_{100} , respectively, and the value of η_{10} is used as a benchmark for comparison. In addition, a Pt was also used as a comparison. The LSV curves for different deposited samples is shown in Fig. S4. At higher concentration of Mn, and thus increasing the participation of Mn ions in the coating formation, the value of η_{10} decreases from 184 mV for the synthesized electrode at a concentration of 10 g.l^{-1} MnCl_2 to 63 mV for the synthesized electrode at a concentration of 70 g.l^{-1} . By increasing the concentration of Mn ions to 100 g.l^{-1} , the value of η_{10} remains almost constant due to the fact that the concentration of Mn in the coating does not change significantly. The synthesized electrode at a concentration of Mn ion of 70 g.l^{-1} is considered as the optimized electrode. For comparison, the LSV curves for NF and Ni-Cu coating generated under similar conditions without Mn ions, and the Pt electrode is shown in Fig. 4a. Obviously, the Pt electrode displays the best behavior with the value of $\eta_{10} = 54 \text{ mV}$. In addition, η_{10} for the Ni-Cu electrode is 152 mV, which is 98 mV higher than the Ni-Cu-Mn electrode, which indicates an improvement in the electrocatalytic behavior due to the alloying and the presence of the Mn element in the coating. Moreover, with slight changes in potential, the amount of current density increases sharply, and to create a current density of 100 mA.cm^{-2} , only 155 mV overpotential is required, which indicates the acceptable kinetics of this electrode. Also, one of the main features of an electrode that reflects its electrocatalytic behavior is the HER kinetics. Here, we studied the kinetic behavior of different electrodes by Tafel analysis. Tafel plots of different electrodes are represented in Fig. 4b. According to the literatures, three different stages can exist for HER in an alkaline environment:⁴⁷



Where, M represents the metallic atom and H_{ads} represents the H atom adsorbed on the active surface of the catalyst. The Volmer step

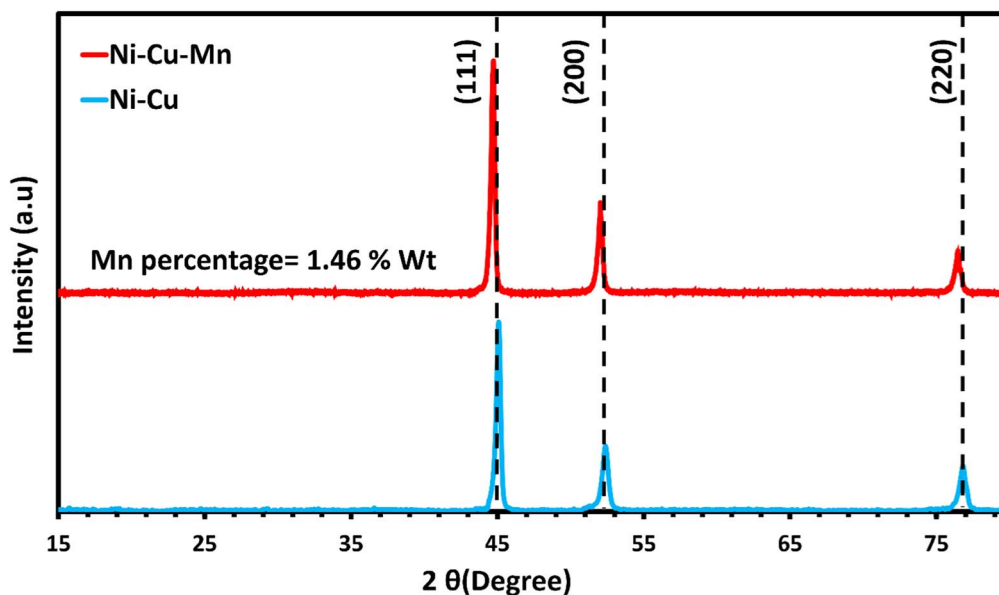


Figure 3. XRD pattern of Ni-Cu and Ni-Cu-Mn electrodes.

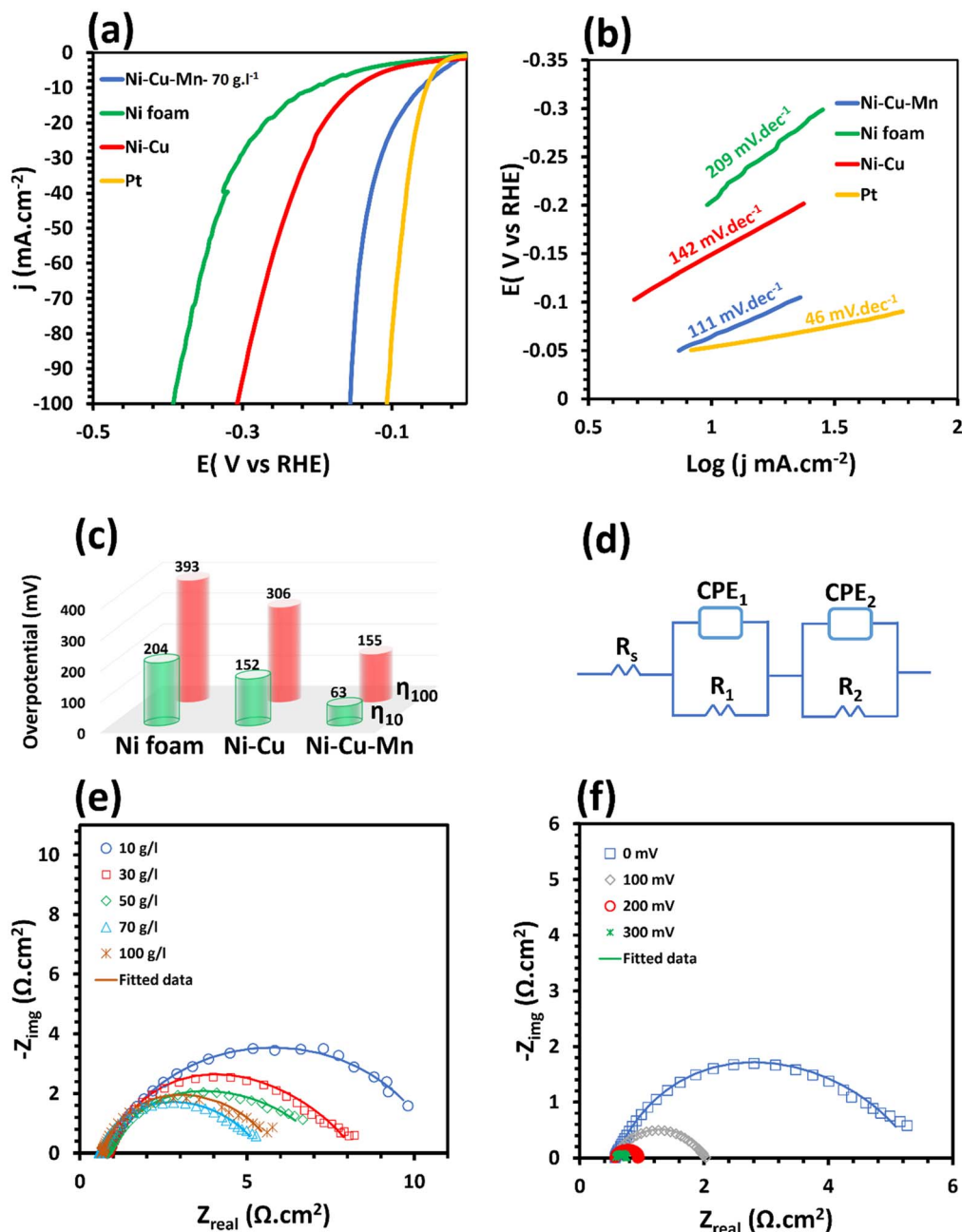


Figure 4. (a) LSV curves of different electrodes with the scan rate of 5 mV.s^{-1} in 1.0 M KOH solution for HER (b) corresponding Tafel plots, (c) required overpotentials at current densities of 10 and 100 mA.cm^{-2} , (d) equivalent circuit used for fitting the EIS data, (e) Nyquist plots of electrodes fabricated at different concentration of MnCl_2 and (f) Nyquist plots of Ni-Cu-Mn electrode fabricated in bath with 70 g.lit^{-1} MnCl_2 at different overpotentials.

represents the electrochemical adsorption of H_{ads} atoms. The Heyrovsky stage is the electrochemical desorption and the Tafel stage is the chemical desorption of hydrogen molecules.⁴⁸ According to the results, it can be seen that the slope value for Ni-Cu is 142 mV.dec^{-1} and for the Ni-Cu-Mn electrode is 111 mV.dec^{-1} , which indicates improvement in the kinetics of the Ni-Cu-Mn electrode. In addition, the HER mechanism in the alkaline medium can be Volmer-Heyrovsky or Volmer-Tafel, and the rate determining stage (RDS) can be determined based on the Tafel slope. The Tafel slope for the Ni-Cu-Mn electrode is 111 mV.dec^{-1} , which is close to 120 mV.dec^{-1} , indicating that the HER mechanism for Ni-Cu-Mn electrode is Volmer-Heyrovsky and the Volmer stage is RDS. Mn doping facilitates the adsorption of H_2O species. Data indicate that the Ni-Cu-Mn is an electrode with excellent electrocatalytic activity and comparable to other non-noble metallic-based electrodes such as

NiMo-NiCu ($\eta_{10} = 86 \text{ mV}$),⁴⁹ NiFe Alloy Nanotube Arrays ($\eta_{10} = 100 \text{ mV}$),⁵⁰ Cu-Co-P ($\eta_{10} = 138 \text{ mV}$),⁵¹ Ni/Cu nanosheet arrays ($\eta_{10} = 38 \text{ mV}$),⁵² NiCoP porous nanosheets ($\eta_{10} = 83 \text{ mV}$),⁵³ Ni-Cu ($\eta_{10} = 76 \text{ mV}$),⁵⁴ Ni-Se-Cu ($\eta_{10} = 136 \text{ mV}$),⁵⁵ NiFeMo ($\eta_{10} = 84.8 \text{ mV}$)⁵⁶ and $\text{Co}_{81}\text{Ni}_{19}$ nanosheet array ($\eta_{10} = 132 \text{ mV}$).⁵⁷

EIS test was used to investigate the charge transfer kinetics in the HER process. The Nyquist curves correspond to different samples coated at different concentrations of Mn ions at a constant overpotential of 0 V vs RHE indicated in Fig. 4e and the Nyquist curves of the sample formed at 70 g.l^{-1} of Mn ions at different overpotentials are represented in Fig. 4f. To study the different mechanisms at the electrode-electrolyte interface, the represented electrical equivalent circuit in Fig. 4d was used. In this equivalent circuit, C_{dl} is replaced by a constant phase element (CPE). Also Here, R_s indicates the solution resistance, CPE_1 and R_1 at the high

frequencies indicate the time-constant of porosities and surface roughness, and CPE_2 and R_2 at the low frequencies is for the time constant of charge transfer process at the electrode-electrolyte interface. The value of R_2 is the charge transfer resistance in the HER process and is an important parameter in the analysis of EIS data. Nyquist curves represent two overlapped semicircles at high and low frequencies. It can be seen that due to the use of a same electrolyte for all samples, the value of R_s (where the curve collides with the x -axis at high frequencies) remains almost constant. According to Fig. 4e, at high frequencies there is no difference between the semicircles circuit, which also indicates that the phase constant at high frequencies is related to surface porosity and roughness. The main difference in the diameter of semicircles is at low frequencies. By increasing the concentration of Mn ions in the coating bath from 10 g.l^{-1} to 70 g.l^{-1} , the amount of R_2 (charge transfer resistance) decrease from $10.3 \Omega.\text{cm}^2$ to the $4.24 \Omega.\text{cm}^2$, indicating that the charge transfer resistance has decreased, which means the better catalytic activity. These results also are in good accordance with the results of the LSV curves. The Nyquist curves of the Ni-Cu-Mn electrode at different overpotentials (Fig. 4f) shows that as the overpotential increases, the amount of charge transfer resistance decreases, which is due to the decrease of activation energy in the HER process and therefore, increase in HER kinetics.

All these results show that electrocatalytic activity is significantly enhanced by incorporation of Mn into Ni-Cu structure. To investigate the reason for this behavior, the electrochemical active surface area (ECSA) of Ni-Cu and Ni-Cu-Mn electrodes was calculated by CV method in none-faradic region at different scan rates and gaining the C_{dl} .^{49,51} CV curves at different scan rates of Ni-Cu and Ni-Cu-Mn (fabricated in 70 g.l^{-1} Mn ions) are shown in Figs. 5a and 5b. In addition, the current density vs scan rate for these electrodes is shown in the Fig. 5c. According to the results, the addition of Mn ions leads to increase in the amount of C_{dl} from 6.1 mF.cm^{-2} for Ni-Cu to 11.3 mF.cm^{-2} for Ni-Cu-Mn electrode. Therefore, the ECSA of Ni-Cu-Mn electrode (565 cm^2) is higher than Ni-Cu (305 cm^2) which approves higher active surface area of Ni-Cu-Mn electrode. Normalization of current density relative to ECSA provides a good metric for comparing intrinsic electrocatalytic behavior.⁵⁸ Therefore, for understanding the outcome of Mn on the intrinsic electrocatalytic behavior, the amount of current in the LSV curve was normalized to the ECSA, which results are shown in Fig. 5d. It is observed that the

incorporation of Mn ions enhance the intrinsic electrocatalytic activity significantly and thus improves the electrocatalytic activity. The intrinsic electrocatalytic activity mechanism improvement due to the Mn ions incorporation can be due to the synergistic effect between different elements. Doping Mn results in electrons being given to nearby Ni and Cu atoms. As a result, the reaction between the Ni and Cu atoms and the H atoms is weakened, which reduces the hydrogen adsorption energy to small values and thus improves the inherent electrocatalytic activity.⁵⁹ In addition, the synergistic effect between the elements modulates the electronic state to improve the electrical conductivity of the catalyst and the H-spillover ability of the electrode.⁴⁶ So, improvement of catalytic activity of Ni-Cu-Mn relative to Ni-Cu electrode can be attributed to enhancement of intrinsic catalytic activity and also increasing the active surface area.

Another unavoidable resistance during the electrolysis process is the bubble resistance, which can greatly affect the electrocatalytic behavior. Hydrogen bubbles formed at the cathode surface can remain on the surface and block the surface, thereby weakening the electrocatalytic activity by reducing the available active sites. The relationship between the surface covered by the bubble and the amount of overpotential is as follows:⁶⁰

$$\eta_\theta = \eta + \log\left(\frac{1}{1-\theta}\right) \quad [9]$$

In which, η_θ is the overpotential affected by bubble formation on the surface, η is the overpotential in the absence of the bubble layer, and θ is the bubble coverage on the surface. As can be seen, with increasing the value of θ , overpotential also increases. So, if a method can be found for the bubbles to detach from the surface as soon as they form, the surface coverage by the bubble layer is reduced and, as a result, the electrocatalytic activity will improve. One effective method is to create a superhydrophilic/superaerophobic nanostructured surface.⁶⁰ These nanostructured surfaces cause the triple phase contact line (TPLC) to become discontinuous, which reduces the adhesion force between the bubble and the surface, and the bubble easily evolved from the surface. Contact angle test was used to evaluate the surface wettability. There is a relationship between water contact angle (θ_w) and bubble contact angle (θ_b) as follows:⁶¹

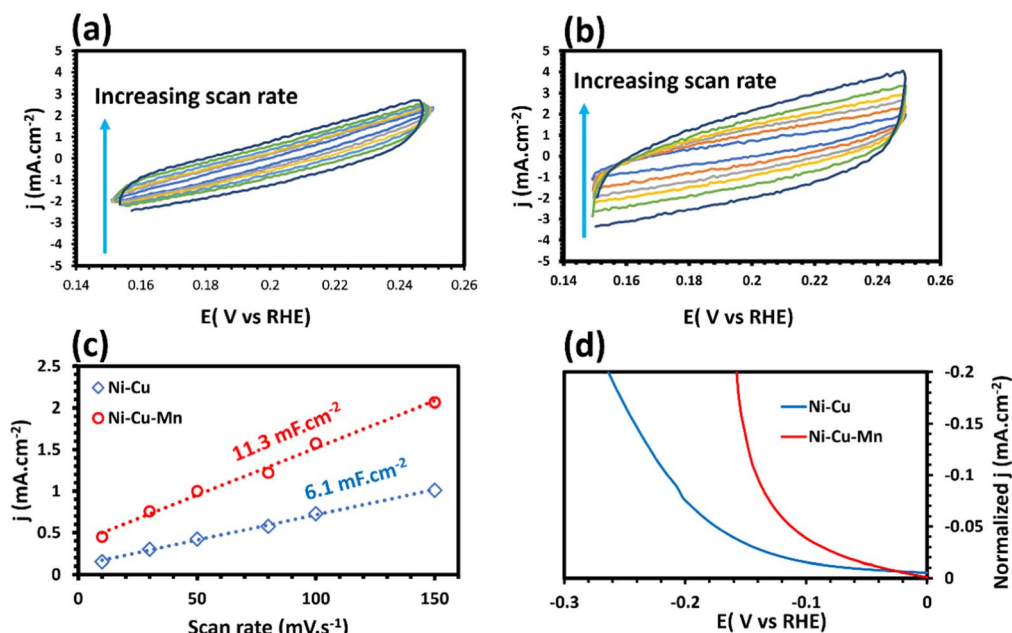


Figure 5. CV curves in none-faradic region at different scan rates of (a) Ni-Cu and (b) Ni-Cu-Mn electrode (fabricated in 70 g.l^{-1} Mn ions), (c) curve of current density as a function of scan rate for calculation of C_{dl} and (d) normalized current density of Ni-Cu and Ni-Cu-Mn electrodes.

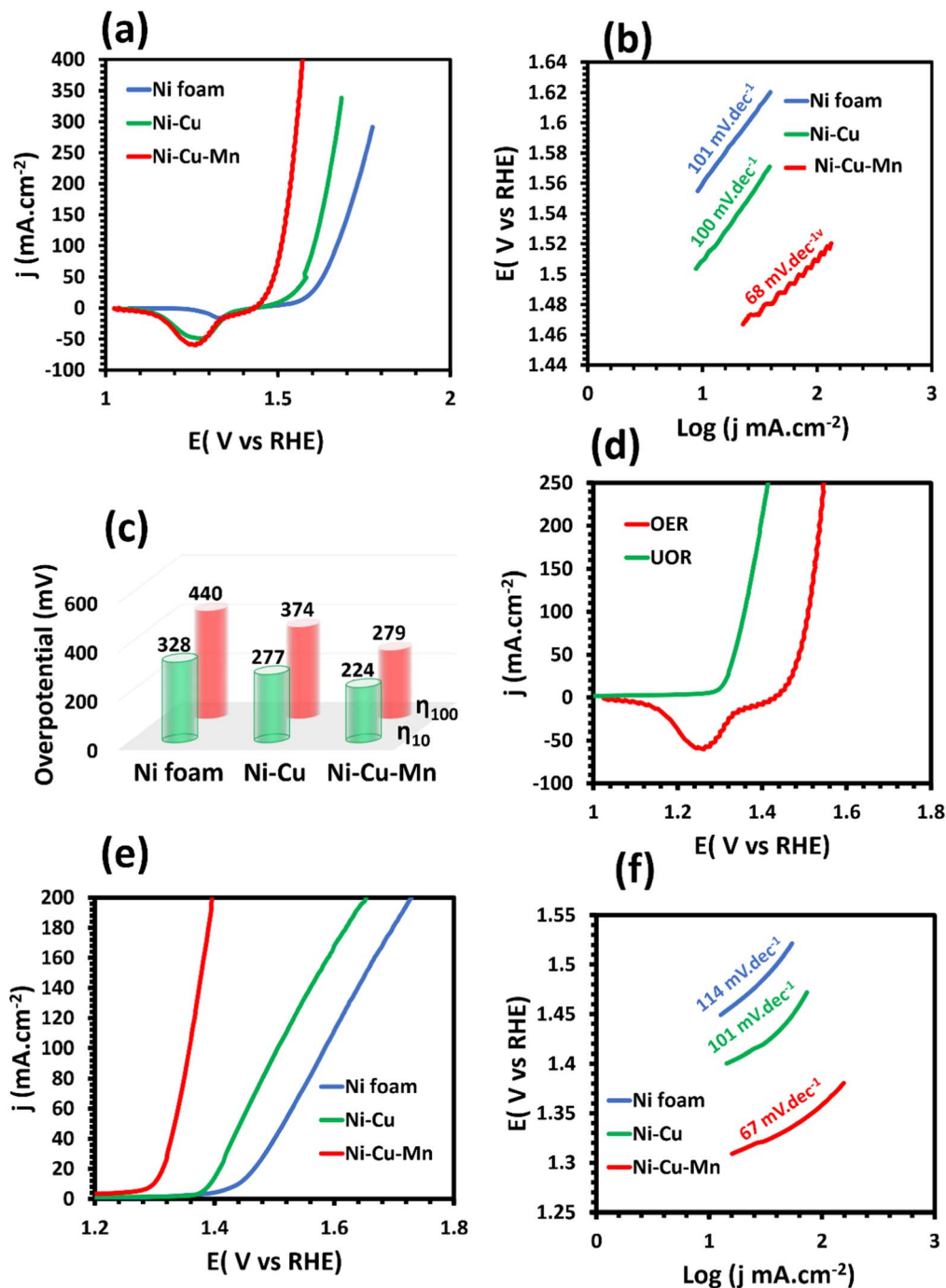


Figure 6. (a) LSV curves of different samples for OER in 1.0 M KOH solution with scan rate of 5 mV.s^{-1} , (b) corresponding Tafel plots, (c) required overpotentials at current densities of 10 and 100 mA.cm^{-2} , (d) LSV curves for comparison of OER and UOR on optimized sample, (e) LSV plots of samples for UOR in 1.0 M KOH + 0.5 M urea solution and (f) corresponding Tafel plots for UOR.

$$\theta_b = 180 - \theta_w \quad [10]$$

According to the above equation, a superhydrophilic surface is a superhydrophobic surface. Contact angle measurement of Ni-Cu-Mn electrode is displayed in Movie S1 which indicates that the water droplet easily penetrates to the electrode surface confirming that the Ni-Cu-Mn electrode is superhydrophilic. These results indicate that one of the main reasons for the excellent properties of the Ni-Cu-Mn electrode is its superhydrophilic/superhydrophobic nature, which reduces the bubble resistance and thus improves the electrocatalytic behavior.

Electrochemical oxygen and urea oxidation reaction.—After investigating the electrocatalytic behavior of the HER process, in this section, we will study the electrocatalytic activity for the OER and UOR processes. In general, the OER process has a slow kinetics because it involves 4-stages of charge transfer and thus reduces the overall kinetics of the overall water splitting process.⁶² The LSV curves of the different samples for investigation of electrocatalytic behavior for OER is shown in Fig. 6a. Also, the Tafel curves is represented in Fig. 6b and also the values of η_{10} and η_{100} for different samples are shown in Fig. 6c. The value of η_{10} for Ni-Cu-Mn electrode is 224 mV, which is much better than Ni-Cu electrode (277 mV), confirming that alloying

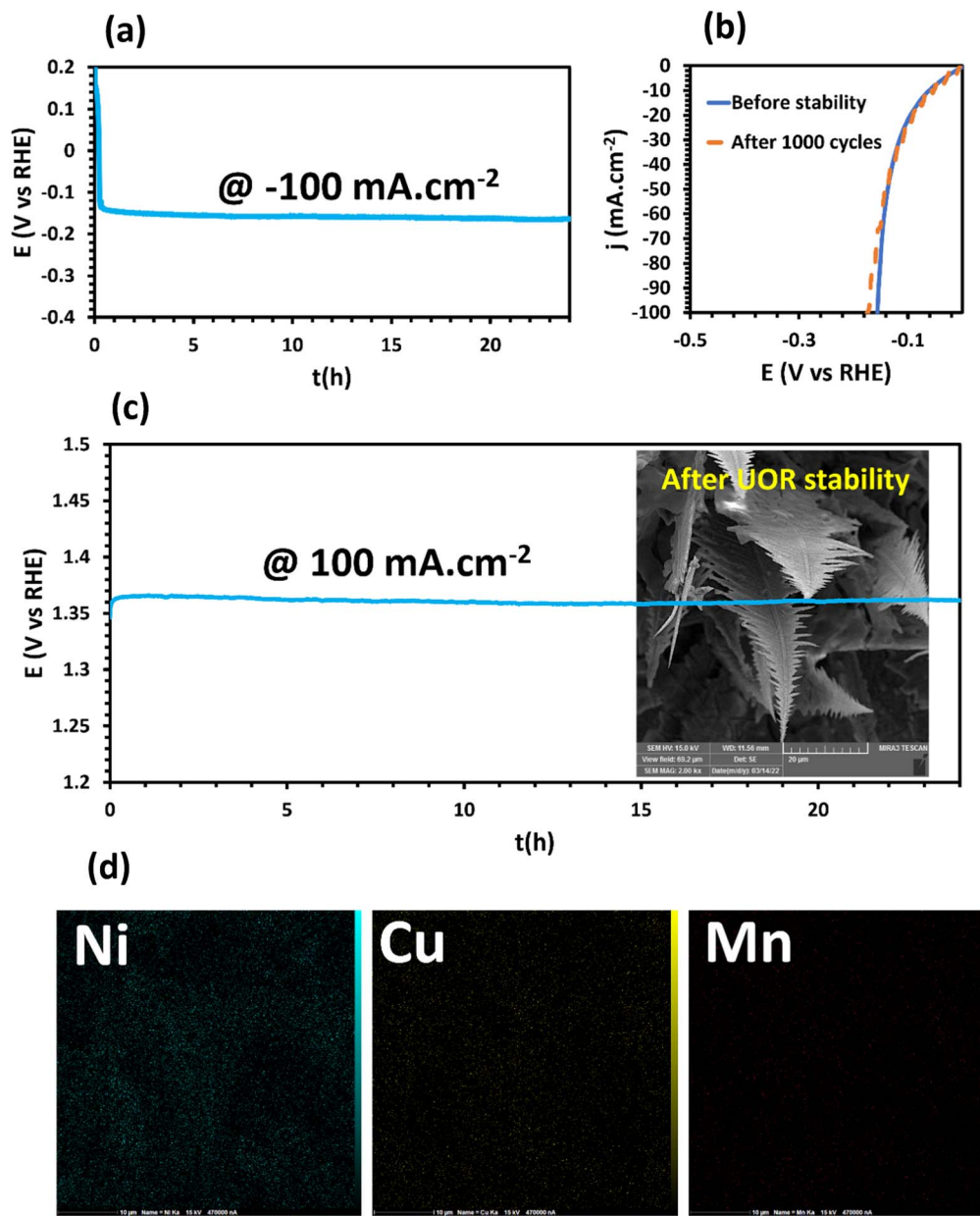


Figure 7. Investigation of electrocatalytic stability of optimized sample for HER and UOR (a) CP plot in applied current density of -100 mA.cm^{-2} for HER, (b) LSV curves before and after 1000 cycles for Ni-Cu-Mn sample, (c) CP plot of optimized sample in applied current density of 100 mA.cm^{-2} for UOR (FESEM image of Ni-Cu-Mn after UOR CP test is inserted in Fig. 6c) and (d) elemental mapping after UOR stability test.

Ni-Cu electrode with Mn leads to improved electrocatalytic behavior. Also, the lower Tafel slope (68 mV.dec^{-1}) of the Ni-Cu-Mn electrode indicates better kinetics of this OER process of this electrode. Low overpotential as well as better kinetics indicate that doping appropriate amounts of Mn in the electrode structure cause significant electrocatalytic activity enhancement. The Ni-Cu-Mn electrode has an acceptable and, in many cases, better electrocatalytic behavior than the none-noble transition metal electrodes reported in the literature such as Nickel-Iron Borophosphate ($\eta_{10} = 215 \text{ mV}$),⁶³ Amorphous Ni-doped CoPi@GC ($\eta_{10} = 320 \text{ mV}$),⁶⁴ NiMoPO $_x$ @NF ($\eta_{10} = 297 \text{ mV}$),⁶⁵ Co-Bi/N-doped carbon@GC ($\eta_{10} = 286 \text{ mV}$),⁶⁶ (CrMnFeCoNi) S_x ($\eta_{100} = 295 \text{ mV}$)⁶⁷ and S-CoTe ($\eta_{10} = 257 \text{ mV}$).⁶⁸

Acceptable electrocatalytic properties of Ni-Cu-Mn electrode for OER process can be attributed to the following factors:

- Increased active-surface area due to the formation of micro-nano dendrites, which leads to an increase in electrochemically active sites.
- Improved intrinsic electrocatalytic properties due to Mn doping within the structure.
- Good wettability of the electrode and thus increase the interface between the electrode and the electrolyte.
- Rapid separation of bubbles from the electrode surface, resulting in reduced bubble resistance.

As it was seen, using the demonstrated strategies, the electrocatalytic activity of the Ni-Cu-Mn electrode for the OER process was improved. But there is still need for high overpotential to produce hydrogen. Conversely, as it was mentioned, the UOR can be a perfect alternative to the OER process. Therefore, to further reduce the cell-voltage value of the water electrolysis process, in this study,

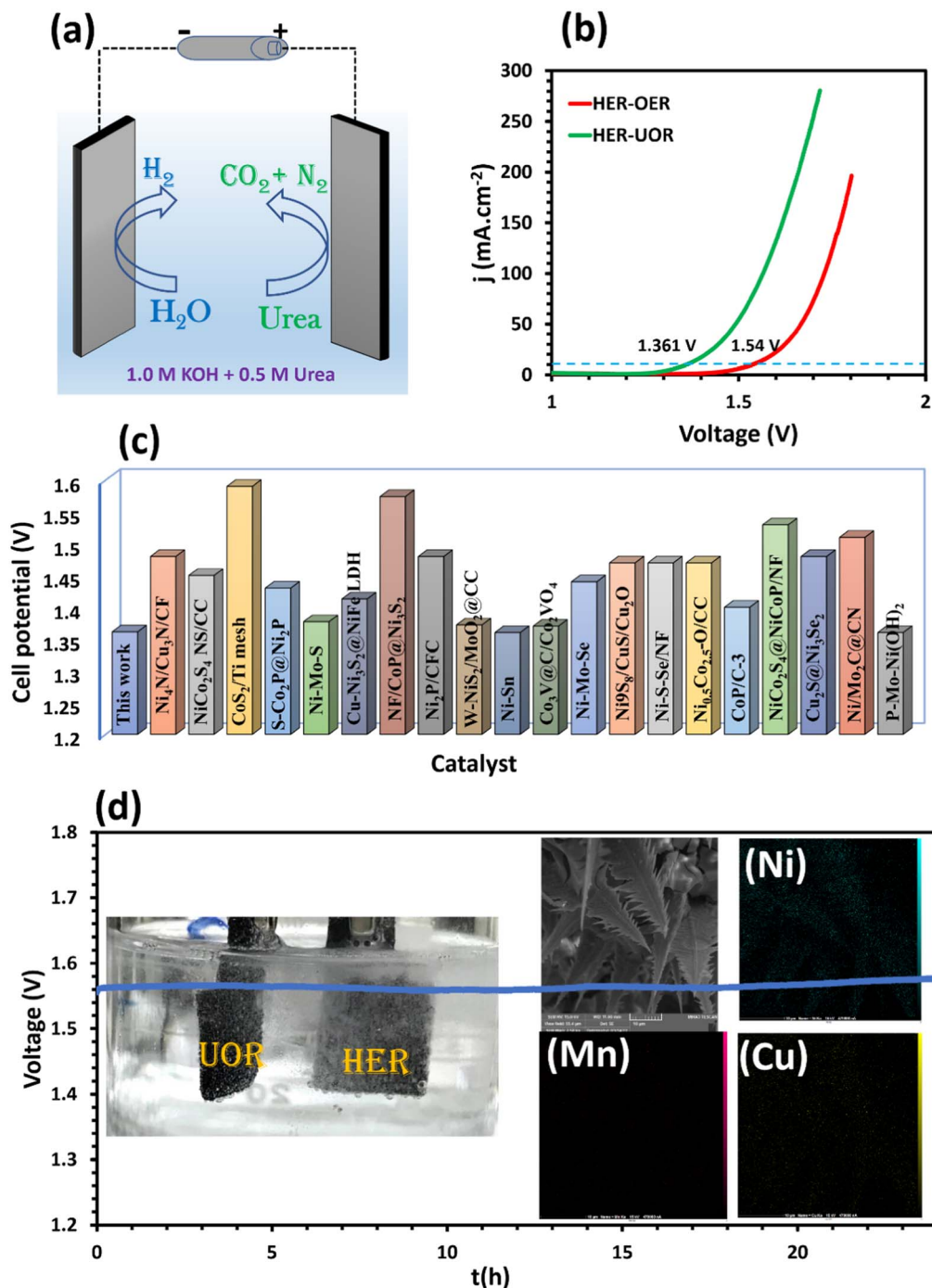


Figure 8. (a) Schematic representation of overall urea-water electrolysis, (b) LSV curves of Ni-Cu-Mn|| Ni-Cu-Mn in two-electrode system of HER-UOR in 1.0 M KOH + 0.5 M urea and HER-OER in 1.0 M KOH solution, (c) Comparison of catalytic performance of Ni-Cu-Mn with other recently published electrodes and (d) CP curve for 2 electrode system recorded at $100 \text{ mA}\cdot\text{cm}^{-2}$ for 24 h (FESEM image and elemental mapping after stability test of Ni-Cu-Mn after stability test is inserted in Fig. 8d).

the OER process was replaced by UOR process with a much lower overpotential. The electrocatalytic behavior of different electrodes was investigated for the UOR process in a solution of 1.0 M KOH + 0.5 M urea in a three-electrode cell. The UOR and OER curves for the optimized electrode are shown in Fig. 6d.

It can be seen that the onset potential of the UOR process is much lower than OER, and also, the potential required to generate a current density of $10 \text{ mA}\cdot\text{cm}^{-2}$ for the UOR process is 1.298 V vs RHE which is 156 mV lower than the OER process (1.454 vs RHE). For comparison, the LSV curves for the NF, Ni-Cu, and Ni-Mn-Cu samples is shown in Fig. 6e. The potential required to generate the

current density of $10 \text{ mA}\cdot\text{cm}^{-2}$ for the Ni-Cu-Mn electrode is 1.298 V vs RHE which is significantly lower than that of the Ni-Cu electrode (1.393 V vs RHE). In addition, the rate in increase in current density due to the increase in overpotential is high, which indicates that the Ni-Cu-Mn electrode is an ideal option for the UOR process. Moreover, the Tafel curves shown in Fig. 6f shows that the Tafel slope of Ni-Cu-Mn ($67 \text{ mV}\cdot\text{dec}^{-1}$) is much lower than Ni-Cu ($101 \text{ mV}\cdot\text{dec}^{-1}$) and NF ($114 \text{ mV}\cdot\text{dec}^{-1}$), that approves the rapid kinetics of the UOR process for Ni-Cu-Mn electrode. In addition, comparison of the electrocatalytic behavior of Ni-Cu-Mn electrode with other recently published studies (Table S1) shows that this

electrode has a comparable and better behavior than other noble metal electrodes. The better electrocatalytic behavior of Ni-Cu-Mn electrode for UOR process can also be due to the creation of a three-dimensional electrode with a high active surface area, synergistic effect between elements, in situ and binder-free electrode formation, as well as the superhydrophilicity of the electrode surface, which increases the existing sites for electrochemical processes as well as the rapid bubble detachment.

Electrochemical stability for HER and UOR.—The stability of electrode during hydrogen production is also important for application in industrial scale. In this study, the electrocatalytic stability of the optimized sample for HER and UOR processes was investigated using chronopotentiometry (CP) and CV tests. CP curve at current density -100 mA.cm^{-2} for 24 h electrolysis and LSV curves before and after 1000 cycles for HER process is represented in Figs. 7a and 7b, respectively. It is observed that after 24 h of electrolysis, the changes in the amount of overpotential is negligible, and also after 1000 cycles, the LSV curve has insignificant change compared to the initial curve, which indicates unique electrocatalytic stability of the Ni-Cu-Mn sample for the HER process. In addition, the result of electrocatalytic stability for the UOR process at a constant current density of 100 mA.cm^{-2} by the CP test in Fig. 7c represents potential change is also negligible, which confirms the exceptional stability of the Ni-Cu-Mn electrode for the UOR process. During the electrocatalytic stability test, severe alkaline conditions as well as the dynamic conditions of gas bubbles detaching from the electrode surface may lead to corrosion or surface damage, which can lead to weakening of the electrocatalytic stability. Therefore, the synthesis method, which does not use any binder during electrochemical deposition process that leads to increased adhesion of the coating to the surface and also favorable electrocatalytic stability, can be the vital reason for better activity and stability. In addition, the chemical composition and morphological stability of the coating can be the main explanations for such stability. To evaluate the morphological stability, the FESEM image and elemental mapping of different elements of the Ni-Cu-Mn electrode surface after UOR electrocatalytic stability test is represented in Figs. 7c and 7d, respectively. The morphological changes after the stability test was very negligible and also, after stability test, the elements distribution was uniform, which confirms the excellent chemical composition and morphological stability. In addition, such morphological stability can be related to nanostructured surface, which leads to the separation of gas bubbles in the smallest diameter. In general, bubbles exert a force on the surface when separated from the surface, which leads to surface destruction.⁶⁹ This force increases with increasing bubble diameter during separation.⁷⁰ As it was seen, the water contact angle of Ni-Cu-Mn micro-nano dendrite was lower than 5° (superhydrophilic surface) and thus based on Eq. 10 it is superaerophobic surface and gas bubbles will easily detach from the surface with smallest diameter. Thus, the resulting nanostructure surface leads to excellent morphological and therefore electrocatalytic stability.

Overall urea-water electrolysis.—Due to the exceptional activity and stability of the Ni-Cu-Mn for both HER and UOR processes, in this part, we examined the overall urea-water electrolysis to efficiently hydrogen production in a two-electrode cell in which the Ni-Cu-Mn electrode (Ni-Cu-Mn || Ni-Cu-Mn) was used as both anode and cathode. Schematic of the overall urea-water electrolysis process is shown in Fig. 8a. For comparison, the overall water splitting process for HER-OER of Ni-Cu-Mn as cathode and anode at same time was also analyzed. Current-cell potential curves for UOR-HER and OER-HER processes is given in Fig. 8b. It can be seen that the cell potential required in the UOR-HER process to generate a current density of 10 mA.cm^{-2} is 1.361 V, which is 179 mV lower than the HER-OER process (1.54 V) that represents the effectiveness of replacing the OER with the UOR process to improve hydrogen production efficiency. The Ni-Cu-Mn electrode also has excellent bi-functional

activity for HER-UOR compared to many electrocatalysts reported in the literature (Fig. 8c and Table S2 for comparison).

In addition, to investigate the electrocatalytic stability of the Ni-Cu-Mn||Ni-Cu-Mn system in a 1.0 M KOH + 0.5 M urea solution, the CP test at an applied current density of 100 mA.cm^{-2} was used for 24 h (Fig. 8d). The results show small changes in the cell potential required to generate a current density of 100 mA.cm^{-2} , indicating excellent electrocatalytic stability. Also, the FESEM images and mapping elements after the stability test given shown in Fig. 8d show that the morphology and chemical composition of the coating remain constant after the stability test, which confirms the morphological and chemical composition stability and consequently the excellent electrocatalytic stability. Good structural stability allows the practical use of this electrode in the processes in which bubbles are produced. Such exceptional activity and stability of the Ni-Cu-Mn in overall urea-water electrolysis system can be due to (1) the synergistic effect between the Ni, Cu and Mn elements in the electrode, which leads to the optimization of the adsorption and desorption path of electro active species. (2) Regular Ni-Cu-Mn nano-microarrays lead to short and direct electron paths, resulting in a decrease in interface resistance. (3) The created three-dimensional structure provides numerous active sites and thus accelerates the process of charge and mass transfer, as well as the diffusion of the created gases. (4) The design of the self-fabricated electrode prevents the addition of any binder to the electrode, which may impair conductivity.

Conclusions

In summary, a simple and cost-effective dynamic hydrogen bubble template method was used to create a Ni-Cu-Mn micro-nano dendritic electrode in this investigation and generated electrode was used for HER and UOR electrocatalysts. The results of microscopic studies indicated the successful formation of Ni-Cu-Mn coating. Also, electrochemical studies show excellent electrocatalytic activity of synthesized electrodes simultaneously for HER and UOR processes. In the HER process, the results showed that the optimized coating is formed in a bath with a concentration of $70 \text{ g.l}^{-1} \text{ MnCl}_2$ in which $\eta_{10} = 63 \text{ mV}$ and $b = 111 \text{ mV.dec}^{-1}$, and also in the UOR process, the required potential to create a current density of 10 mA.cm^{-2} was 1.298 V vs RHE. Also, Ni-Cu-Mn electrode was used as a bi-functional electrode for HER and UOR processes in the two-electrode system. The results showed that in this system, in order to create a current density of 10 mA.cm^{-2} , the cell potential was only 1.361 V. The results of electrocatalytic stability studies by CP and CV methods also showed the excellent electrocatalytic stability of this electrode. Such unique electrocatalytic performance for HER and UOR can be due to low charge transfer resistance, high ECSA value, excellent inherent electrocatalytic activity and the superhydrophilicity nature. This study is a unique attempt to synthesize transition metallic based electrocatalysts for urea-assisted hydrogen production.

Acknowledgments

Naser Lotfi was supported by a grant from Ferdowsi University of Mashhad (No.FUM-62298).

ORCID

Gh. Barati Darband  <https://orcid.org/0000-0002-9918-7869>

References

1. J.-Y. Zhang, T. He, M. Wang, R. Qi, Y. Yan, Z. Dong, H. Liu, H. Wang, and B. Y. Xia, *Nano Energy*, **60**, 894 (2019).
2. T. Liu, X. Zhang, T. Guo, Z. Wu, and D. Wang, *Electrochim. Acta*, **334**, 135624 (2020).
3. X. Zhang, T. Liu, T. Guo, Z. Mu, X. Hu, K. He, X. Chen, V. P. Dravid, Z. Wu, and D. Wang, *ACS Appl. Mater. Interfaces*, **13**, 40705 (2021).
4. D. Wang, T. Liu, J. Wang, and Z. Wu, *Carbon*, **139**, 845 (2018).
5. D. Guo, D. Duan, J. Gao, X. Zhou, S. Liu, and Y. Wang, *Int. J. Hydrogen Energy*, **47**, 6620 (2022).

6. X. Liu, J. Niu, S. Rajendran, Y. Lei, J. Qin, and X. Zhang, *Int. J. Hydrogen Energy*, **46**, 27495 (2021).
7. Z. Zhang, Y. Wu, and D. Zhang, *Int. J. Hydrogen Energy*, **47**, 1425 (2022).
8. X. Zhang, J. Wang, T. Guo, T. Liu, Z. Wu, L. Cavallo, Z. Cao, and D. Wang, *Appl. Catalysis B*, **247**, 78 (2019).
9. H. Xu, J. Cao, C. Shan, B. Wang, P. Xi, W. Liu, and Y. Tang, *Angew. Chem.*, **130**, 8790 (2018).
10. H. Sun, W. Zhang, J.-G. Li, Z. Li, X. Ao, K.-H. Xue, K. K. Ostrikov, J. Tang, and C. Wang, *Appl. Catalysis B*, **284**, 119740 (2021).
11. C. Li, Y. Liu, Z. Zhuo, H. Ju, D. Li, Y. Guo, X. Wu, H. Li, and T. Zhai, *Adv. Energy Mater.*, **8**, 1801775 (2018).
12. Y. Ding, X. Du, and X. Zhang, *Appl. Surf. Sci.*, **584**, 152622 (2022).
13. M. Maleki, G. B. Darband, A. S. Rouhaghdam, R. Andaveh, and Z. M. Kazemi, *Chem. Commun.*, **58**, 3545 (2022).
14. G. B. Darband, N. Lotfi, A. Aliabadi, S. Hyun, and S. Shanmugam, *Electrochim. Acta*, **382**, 138335 (2021).
15. H. Sarno, E. Ponticorvo, and D. Scarpa, *Chem. Eng. J.*, **377**, 120600 (2019).
16. H. Begum, M. S. Ahmed, D.-W. Lee, and Y.-B. Kim, *Sci. Rep.*, **9**, 1 (2019).
17. P. Xiong, X. Ao, J. Chen, J.-G. Li, L. Lv, Z. Li, M. Zondode, X. Xue, Y. Lan, and C. Wang, *Electrochim. Acta*, **297**, 833 (2019).
18. B. Zhu, Z. Liang, and R. Zou, *Small*, **16**, 1906133 (2020).
19. A. Schranck, R. Marks, E. Yates, and K. Doudrick, *Environmental science & technology*, **52**, 8638 (2018).
20. J. Li, C. Yao, X. Kong, Z. Li, M. Jiang, F. Zhang, and X. Lei, *Acs Sustainable Chemistry & Engineering*, **7**, 13278 (2019).
21. S. Lu, M. Hummel, Z. Gu, Y. Wang, K. Wang, R. Pathak, Y. Zhou, H. Jia, X. Qi, and X. Zhao, *ACS Sustainable Chemistry & Engineering*, **9**, 1703 (2021).
22. R.-Y. Ji, D.-S. Chan, J.-J. Jow, and M.-S. Wu, *Electrochem. Commun.*, **29**, 21 (2013).
23. G. Barati Darband, M. Aliofkhazraei, S. Hyun, and S. Shanmugam, *ACS Appl. Mater. Interfaces*, **12**, 53719 (2020).
24. N. Lotfi, T. Shahrabi, Y. Yaghoobinezhad, and G. B. Darband, *Electrochim. Acta*, **326**, 134949 (2019).
25. S. Peng, F. Gong, L. Li, D. Yu, D. Ji, T. Zhang, Z. Hu, Z. Zhang, S. Chou, and Y. Du, *JACS*, **140**, 13644 (2018).
26. C. Wu, H. Li, Z. Xia, X. Zhang, R. Deng, S. Wang, and G. Sun, *ACS Catal.*, **10**, 11127 (2020).
27. Q. Li, W. Zhang, J. Shen, X. Zhang, Z. Liu, and J. Liu, *J. Alloys Compd.*, **902**, 163670 (2022).
28. M. Arabi, A. Ghaffarinejad, and G. B. Darband, *J. Electroanal. Chem.*, **907**, 116066 (2022).
29. Y. Tong, L. Chen, P. J. Dyson, and Z. Fei, *J. Mater. Sci.*, **56**, 17709 (2021).
30. H. Wang, H. Zhou, W. Zhang, and S. Yao, *J. Mater. Sci.*, **53**, 8951 (2018).
31. Y. Yang, H. Meng, C. Kong, S. Yan, W. Ma, H. Zhu, F. Ma, C. Wang, and Z. Hu, *J. Colloid Interface Sci.*, **599**, 300 (2021).
32. L. Liu, X. Liu, and S. Jiao, *J. Colloid Interface Sci.*, **564**, 77 (2020).
33. X. Lu and C. Zhao, *Nat. Commun.*, **6**, 1 (2015).
34. J. Hassoun, S. Panero, P. Simon, P. L. Taberna, and B. Scrosati, *Adv. Mater.*, **19**, 1632 (2007).
35. M. Maleki, A. Sabour Rouhaghdam, G. Barati Darband, D. Han, and S. Shanmugam, *ACS Appl. Energy Mater.*, **5**, 2937 (2022).
36. F. Wang, K. Zhang, Q. Zha, and Y. Ni, *J. Alloys Compd.*, **899**, 163346 (2022).
37. M. Zhang, H. Du, Z. Wei, X. Zhang, and R. Wang, *ACS Appl. Energy Mater.*, **4**, 8262 (2021).
38. S. Sirisomboonchai, N. Kitiphatpiboon, M. Chen, S. Li, X. Li, S. Kongparakul, C. Samart, L. Zhang, A. Abudula, and G. Guan, *ACS Appl. Energy Mater.*, **5**, 149 (2021).
39. H. Yang, M. Yuan, D. Wang, Z. Sun, H. Li, and G. Sun, *ACS Appl. Energy Mater.*, **4**, 8563 (2021).
40. F. Wang, X. Guo, F. He, Y. Hou, F. Liu, C. Zou, and H. Yang, *Sustainable Energy & Fuels*, **6**, 851 (2022).
41. M. Hao, V. Charbonneau, N. Fomena, J. Gaudet, D. Bruce, S. Garbarino, D. A. Harrington, and D. Guay, *ACS Appl. Energy Mater.*, **2**, 5734 (2019).
42. S. Vesztorgom, A. Dutta, M. Rahaman, K. Kiran, I. Zelocualtecatl Montiel, and P. Broekmann, *ChemCatChem*, **13**, 1039 (2021).
43. B. J. Plowman, L. A. Jones, and S. K. Bhargava, *Chem. Commun.*, **51**, 4331 (2015).
44. Y. Liu and S. Dillon, *Chem. Commun.*, **50**, 1761 (2014).
45. S. Khorsand, K. Raeissi, F. Ashrafizadeh, and M. Arenas, *Surf. Coat. Technol.*, **276**, 296 (2015).
46. A. Nairan, P. Zou, C. Liang, J. Liu, D. Wu, P. Liu, and C. Yang, *Adv. Funct. Mater.*, **29**, 1903747 (2019).
47. P. Asen, A. Esfandiari, and H. Mehdipour, *Nanoscale*, **14**, 1347 (2022).
48. S. Ye, F. Luo, T. Xu, P. Zhang, H. Shi, S. Qin, J. Wu, C. He, X. Ouyang, and Q. Zhang, *Nano Energy*, **68**, 104301 (2020).
49. H. L. Santos, P. G. Corradini, M. Medina, J. A. Dias, and L. H. Mascaro, *ACS Appl. Mater. Interfaces*, **12**, 17492 (2020).
50. C.-L. Huang, X.-F. Chuah, C.-T. Hsieh, and S.-Y. Lu, *ACS Appl. Mater. Interfaces*, **11**, 24096 (2019).
51. Y. S. Park, W.-S. Choi, M. J. Jang, J. H. Lee, S. Park, H. Jin, M. H. Seo, K.-H. Lee, Y. Yin, and Y. Kim, *ACS Sustainable Chemistry & Engineering*, **7**, 10734 (2019).
52. S. Li, M. Li, and Y. Ni, *Appl. Catalysis B*, **268**, 118392 (2020).
53. Y. Jia, L. Zhu, H. Pan, Y. Liao, Y. Zhang, X. Zhang, Z. Jiang, M. Chen, and K. Wang, *Appl. Surf. Sci.*, **580**, 152314 (2022).
54. J. Niu, Y. Yue, C. Yang, Y. Wang, J. Qin, X. Zhang, and Z.-S. Wu, *Appl. Surf. Sci.*, **561**, 150030 (2021).
55. Y. Gao, Y. Wu, H. He, and W. Tan, *J. Colloid Interface Sci.*, **578**, 555 (2020).
56. Z. Lv, Z. Li, X. Tan, Z. Li, R. Wang, M. Wen, X. Liu, G. Wang, G. Xie, and L. Jiang, *Appl. Surf. Sci.*, **552**, 149514 (2021).
57. C. Cheng, F. Zheng, C. Zhang, C. Du, Z. Fang, Z. Zhang, and W. Chen, *J. Power Sources*, **427**, 184 (2019).
58. H. Xu, Y. Liao, Z. Gao, Y. Qing, Y. Wu, and L. Xia, *J. Mater. Chem. A*, **9**, 3418 (2021).
59. T. Liu, X. Ma, D. Liu, S. Hao, G. Du, Y. Ma, A. M. Asiri, X. Sun, and L. Chen, *ACS Catal.*, **7**, 98 (2017).
60. R. Andaveh, G. B. Darband, M. Maleki, and A. S. Rouhaghdam, *J. Mater. Chem. A*, **10**, 5147 (2022).
61. W. Y. L. Ling, G. Lu, and T. W. Ng, *Langmuir*, **27**, 3233 (2011).
62. N.-T. Suen, S.-F. Hung, Q. Quan, N. Zhang, Y.-J. Xu, and H. M. Chen, *Chem. Soc. Rev.*, **46**, 337 (2017).
63. J. Kwon, H. Han, S. Jo, S. Choi, K. Y. Chung, G. Ali, K. Park, U. Paik, and T. Song, *Adv. Energy Mater.*, **11**, 2100624 (2021).
64. L. Yang, H. Ren, Q. Liang, K. N. Dinh, R. Dangol, and Q. Yan, *Small*, **16**, 1906766 (2020).
65. F. Kong, L. Sun, L. Huo, and H. Zhao, *J. Power Sources*, **430**, 218 (2019).
66. Q. Hu, G. Li, Z. Han, Z. Wang, X. Huang, X. Chai, Q. Zhang, J. Liu, and C. He, *Adv. Energy Mater.*, **9**, 1901130 (2019).
67. M. Cui, C. Yang, B. Li, Q. Dong, M. Wu, S. Hwang, H. Xie, X. Wang, G. Wang, and L. Hu, *Adv. Energy Mater.*, **11**, 2002887 (2021).
68. L. Yang, H. Qin, Z. Dong, T. Wang, G. Wang, and L. Jiao, *Small*, **17**, 2102027 (2021).
69. G. B. Darband, M. Aliofkhazraei, and S. Shanmugam, *Renew. Sustain. Energy Rev.*, **114**, 109300 (2019).
70. G. B. Darband, M. Aliofkhazraei, S. Hyun, A. S. Rouhaghdam, and S. Shanmugam, *J. Power Sources*, **429**, 156 (2019).